Exploring the tunable micro-/macro-structure enabled by alginate-gelatin bioinks for tissue engineering

Lucas Lemarié, Jérôme Sohier, Edwin-Joffrey Courtial

Biomedical Engineering Advances 8 (2024) 100135

Contents lists available at ScienceDirect

Biomedical Engineering Advances

journal homepage: www.journals.elsevier.com/biomedical-engineering-advances

Exploring the tunable micro-/macro-structure enabled by alginate-gelatin bioinks for tissue engineering

Lucas Lemarié [a,b,c,*], Jérôme Sohier [b], Edwin-Joffrey Courtial [c]

[a] SEGULA Technologies, 69100 Villeurbanne, France
[b] CNRS UMR 5305, LBTI (Tissue Biology and Therapeutic Engineering Laboratory), 69007 Lyon, France
[c] 3dFAB, CNRS UMR 5246, ICBMS (Institute of Molecular and Supramolecular Chemistry and Biochemistry), Université Lyon 1, 69622 Villeurbanne, France

ARTICLE INFO

Keywords:
Bioprinting
High conservation
Exceedingly adaptable viscoelastic properties
Tunable microstructure

ABSTRACT

This study explores the development of optimized alginate-gelatin (AG) bioinks for advanced 3D bioprinting applications, particularly in tissue engineering. Central to our investigation is the establishment of a method for producing AG bioinks with highly tunable viscoelastic properties and the ability to create both macro- and microporous scaffolds through a liquid-liquid emulsion technique applied to chemically crosslinked hydrogels and shaped by microextrusion. Our methodology encompasses a comprehensive evaluation of homogenization, pasteurization techniques, and rheological assessments to optimize the mechanical properties of AG hydrogels, ensuring their suitability for bioprinting.

The study demonstrates that dynamic homogenization and conventional pasteurization methods yield superior dissolution and sterility of the bioinks, crucial for maintaining optical quality and biological compatibility. Crosslinking optimization significantly enhanced the elasticity and reduced post-crosslinking shrinkage of the hydrogels, a key factor in achieving desired cell viability and function within the engineered tissues. The incorporation of porosity through a controlled liquid-liquid emulsion process was found to enhance cellular interactions and integration within the bioprinted constructs.

Our findings confirm that the rheological properties of bioinks play a crucial role in determining bioprintability, with temperature modulation emerging as a key tool for tailoring these characteristics. The biocompatibility and functional performance of the AG hydrogels were validated through in vitro experiments, demonstrating promising cell viability and proliferation. This research lays the groundwork for the development of advanced bioinks capable of supporting complex tissue architectures in regenerative medicine and tissue engineering. By marrying the versatility of alginate and gelatin with innovative fabrication techniques, our study advances the frontier of 3D bioprinting, paving the way for the creation of biomimetic tissues with enhanced physiological relevance and therapeutic potential.

1. Introduction

Bioinks play a pivotal role in advancing 3D bioprinting and tissue engineering, offering a promising avenue for creating complex and functional bioengineered tissues [1,2]. There are a large number of biomaterials, such as hyaluronic acid (natural) or polyethylene glycol (synthetic), that have shown great potential for both regenerative medicine and for the formation of pathological models or even diagnostic tools [3-5]. Among these, alginate-gelatin (AG) bioinks stand out for their remarkable biocompatibility, widespread utilization, and relevance in crafting bioengineered tissues [6]. Their properties enable to tailor viscoelastic properties and optimize macro and microporosity [7], a critical factor essential for optimal tissue maturation, in opposition to solid hydrogels [8,9].

The significance of a multiscale approach cannot be overstated. Adjustment of macrostructure using bioprinting allows customized architecture, enhanced cell viability, and improved tissue integration [10, 11]. Alongside, modulation of microstructure boosts cell infiltration, mass transport, nutrient diffusion, and optimizes surfaces for cell anchoring [12-14].This dual approach underscores the importance of achieving optimal biological responses by promoting cell viability, differentiation, and the formation of a functional extracellular matrix,

* Corresponding author.
E-mail addresses: lucas.lemarie@segula.fr (L. Lemarié), jerome.sohier@cnrs.fr (J. Sohier), edwin.courtial@univ-lyon1.fr (E.-J. Courtial).

https://doi.org/10.1016/j.bea.2024.100135
Received 29 April 2024; Received in revised form 11 September 2024; Accepted 18 September 2024
Available online 4 October 2024

towards the creation of bioengineered tissues with improved physiological relevance and functionality [15].

A plethora of methods exist to induce porosity in a pre-crosslinked hydrogel, such as the salt leaching method [16], temperature-sensitive beads inclusion [17] or freeze-drying [18]. Additionally, it is possible to induce porosity during crosslinking, by employing effervescence for example [19]. When the hydrogel is still in the stage of Newtonian liquid or viscoelastic fluid (pre-crosslinking) microstructure modulation is possible, notably by including air (foaming) [20] or emulsifying with a second material (emulsion) [21,22]. However, these porosity induction approaches are inherently limited in microextrusion bioprinting since none are compatible with maintaining cell survival and rheological properties (flow threshold), to ensure tissue maturation and shape fidelity. For instance, the previously described methods are intrinsecally incompatible with microextrusion due to the necessity of cell incorporation after crosslinking [23]. To date, only one approach described in the literature (Aqueous Two Thase Emulsion, ATPS) allows hydrogels to modulate their microstructure by performing bioprinted scaffold through photoreticulation [24].

In this study, we propose a method for producing AG bioinks with (i) highly tunable viscoelastic properties and (ii) both macro and microporous scaffolds through the liquid-liquid emulsion technique applied to chemically crosslinked hydrogels and shaped by microextrusion. To begin, our initial focus is on optimizing the processes of homogenization and pasteurization by comparing various techniques. Following this, we delve into examining the adjustable mechanical properties of both porous and non-porous AG hydrogels. Subsequently, we analyze their rheological properties to assess how suitable they are for bioprinting. Finally, we showcase the advantages of porous Alginate-Gelatin hydrogels with fibroblast cells through bioprinting experiments.

2. Materials and methods

2.1. Alginate–Gelatin hydrogels preparation and cross-linking

- Hydrogels ratio and concentration

Three Alginate-Gelatin hydrogels (AG-nX with n=1, 3 or 5) were prepared by powder dissolution according to Table 1, based on a 1:2 ratio of alginate to gelatin in Dulbecco's Phosphate Buffered Saline (DPBS) to maintain a single concentration factor as the variable among the formulations.

- Mechanical and thermal agitation

To compare powder dissolution methods, 20 mL of each AG-nX (n=1,3,5) formulation was prepared. To achieve this, 10 g of sodium alginate (120–190 kDa, 39% guluronic acid, 180,947–100 G, Sigma, USA) and 20 g of gelatin (40–100 kDa, type B, G9382, Sigma, USA) were mixed in a Falcon 50 tube. From this mixture, 0.3 g (AG-1X), 0.9 g (AG-3X), and 1.5 g (AG-5X) were weighed and deposited into 10 mL of DPBS (Thermo Scientific, USA) to obtain the AG-nX (n=1,3,5) formulations (Table 1).

For the **classical dissolution** method, the powder mixture was prepared under a laminar flow hood by pouring the powders and PBS into a Falcon 50 tube. The tubes were then incubated at 37 °C at least 4 hours in static conditions.

Table 1
Description of AG-nX (n=1, 3, 5) formulations concentration w/v of alginate and gelatin in DPBS.

Name (AG-nX)	Alginate (w/v)	Gelatin (w/v)
AG-1X	1%	2%
AG-3X	3%	6%
AG-5X	5%	10%

For the **dynamic dissolution** method, the powder mixture was prepared in a 25 mL Erlenmeyer flask, where the powders and DPBS were placed along with a magnetic stir bar. Erlenmeyer flasks were sealed with an aluminum cap and subjected to agitation (50 RPM, 60 °C for 120 min) to facilitate powder dissolution.

- Pasteurization

Regarding the sterilization of formulations AG-nX (x=1,3,5), two pasteurization methods were applied to samples obtained through the dynamic method (50 RPM, 60 °C for 120 min). A **rapid method** (100 °C for 10 min, 50 RPM) and a **conventional method** (80 °C for 30 min, 50 RPM), both followed by a thermal shock in water at 0 °C for 10 min in both cases. Following pasteurization, the hydrogels were stored at 4 °C for subsequent use for up to 4 weeks. The quality of sterilization was assessed by culturing the gels in DMEM culture medium maintained in the incubator (37 °C, 5% CO2) for 72 hours, without the appearance of bacterial or yeast contamination.

- Crosslinking

Crosslinking solution by dissolving 1% w/v of calcium chloride $CaCl_2$ (Sigma, USA) and 1% w/v transglutaminase (TAG) (Ajinomoto, Japan) powder in ultrapure water. The crosslinking mechanisms of these two agents are depicted in the Fig. 1-A.

Following printing, AG-nX scaffolds (x=1,3,5) were placed at 4 °C for 10 minutes to allow for hydrogel gelation. The crosslinking solution was subsequently deposited for 10 minutes at 37 °C. To perform crosslinking, calcium ions Ca^{2+} induce the chelation of alginate according to the egg-box structure [25], while gelatin enables the covalent binding of gelatin units with TAG [26] enabling the formation of a interpenetrating double network. After crosslinking and rinsing, the combination of scaffolding (macropores) and ATPS (micropores) induces multi-scale porosity in the bio-printed object (Fig. 1-B). The method for inducing microporosity is described in the "2. Hydrogel porosity induction" section.

2.2. Hydrogel porosity induction

To induce porosity in the hydrogels, a liquid-liquid emulsion method was employed [24,27]. Briefly, a sterile solution of PolyEthylene Glycol (PEG) 20 kDa (Sigma, USA) was prepared by dissolving 0.5 g in 1 mL of distilled water (50%, w/v) under mechanical stirring for 30 minutes (this solution will be referred to as PEG50 in the rest of the study). The PEG50 solution was then added to the AG-nX formulations at volume ratios (v/v) of 5%, 10%, and 20% and emulsification was performed through 10 suction-reflow in a 1.5 mL Eppendorf tube, using a 100µL positive displacement pipet (Microman™, Thermofisher, Franklin, MA, USA) at 15 °C for AG-1X, 25 °C for AG-3X, and 35 °C for AG-5X to achieve isoviscosity emulsion before crosslinking as previously described. To investigate the relationship between emulsion quality and hydrogel temperature, emulsification at a 10% v/v ratio was also performed on AG-3X at 10 °C, 25 °C, and 37 °C. **The resulting porous hydrogels are denoted with an asterisk (AG-nX*) to distinguish them from the dense hydrogel (AG-nX).**

2.3. Structural characterization

- **Scanning Electron Microscopy (SEM)**

AG-nX and AG-nX* (n=1,3,5) discs (20 mm in diameter and 1 mm in thickness) were crafted, crosslinked and subsequently cryogenically frozen in liquid nitrogen for 10 min. Then, AG-nX (n=1,3,5) discs underwent controlled fracture between two smooth metal jaws, employing mechanical impact to reveal their microstructure devoid of any cutting-induced artifacts. Sample were then analyzed by Scanning Electron Microscope (SEM) (TM4000, Hitachi, Tokyo, Japan) at 10 kV, utilizing

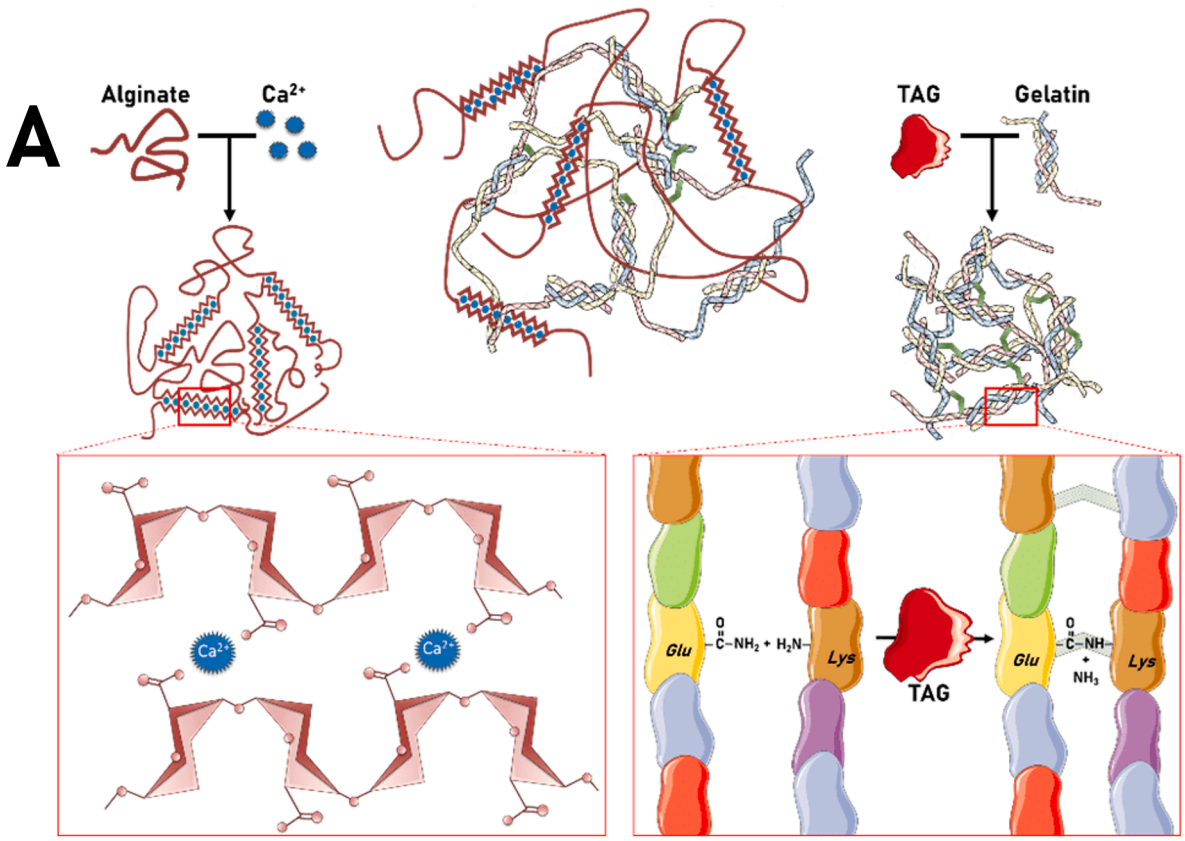

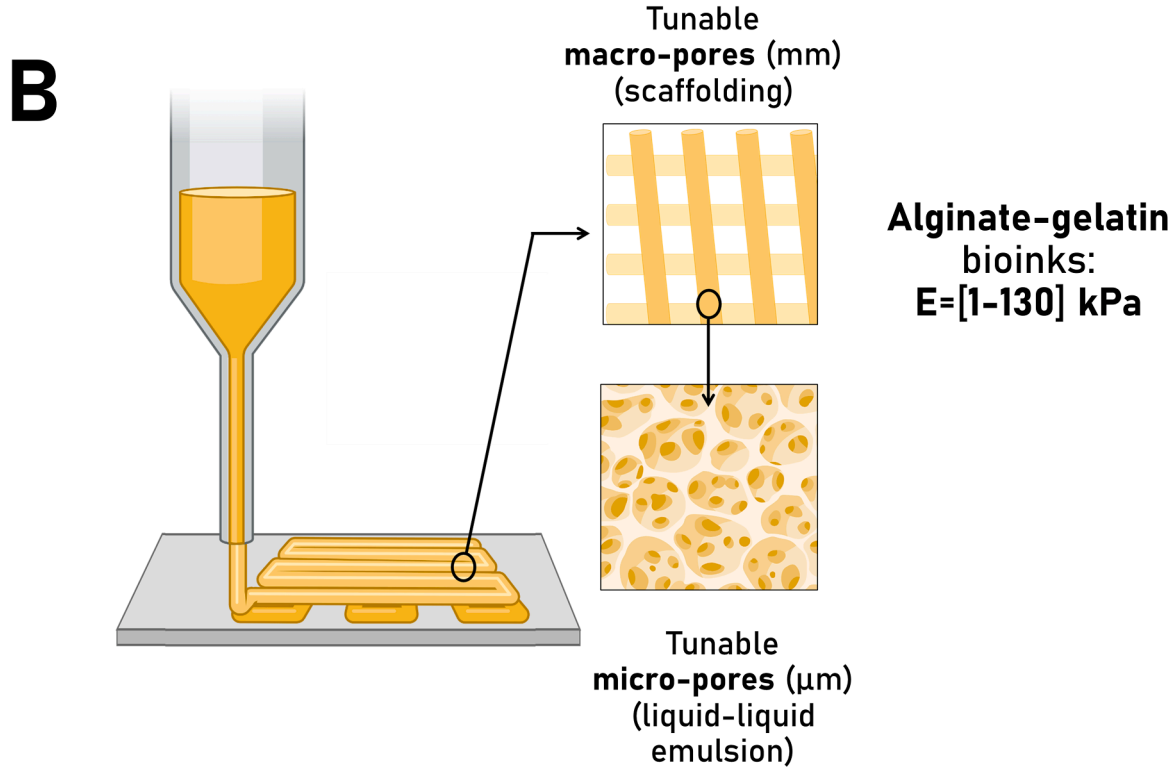

Fig. 1. Alginate-Gelatin crosslinking and study global strategy. (A) Crosslinking phenomenon using ionic (chelation by Ca^{2+}) and covalent reactions (enzymatic bonding by transglutaminase (TAG)) (B) Production of micro-/macro-porous scaffold through microextrusion bioprinting with alginate-gelatin bioinks.

backscattered electron (BSE) mode at 20X and 100X magnification.

· **Swelling**

The swelling capacity of the AG-nX (n=1, 3, 5) formulations was determined based on the rehydration of lyophilized discs [28]. Briefly, three 2 mL discs of each hydrogel were prepared by molding in a 12-well plate and then crosslinked after gelation at 4 °C for 15 minutes.

After weighing to obtain the hydrated weight (Wh), the samples were lyophilized overnight (Wd) and rehydrated in DPBS at 37 °C followed by recurrent weighing. The samples were weighed on a precision balance (XPR204S, Mettler Toledo, US) and the swelling capacity of the hydrogels was calculated at different time based on the following Eq. (1):

$$\textit{Swelling ratio}\ (\%) = \frac{(Wh - Wd)}{Wh} \times\ 100 \quad (1)$$

· **Degradation test**

A hydrolytic degradation test was conducted on the AG-nX (n=1, 3, 5) formulations over a period of 28 days in DPBS in triplicate. After an initial weighting (Wi), hydrogels were immersed in DPBS and incubated at 37 °C to simulate cell culture conditions. Mass loss was monitored by precise weighing at predetermined intervals throughout the 28-day period (Wt). At each time point, the hydrogels were removed from the DPBS, gently blotted to remove excess liquid, and weighed using an analytical balance with a precision of 0.001 gs. The percentage of mass loss was calculated at different time based on the following Eq. (2):

$$\textit{Weight loss}\ (\%) = 100 - \frac{(Wi - Wt)}{Wi} \times\ 100 \quad (2)$$

2.4. Rheological & mechanical behaviours characterization

A stress-controlled rotational rheometer (DHR2, TA instruments, USA) was used to investigate the rheological properties of the AG-nX and AG-nX* (n=1,3,5) formulations before and after crosslinking. Before crosslinking, a flow sweep procedure was performed with Peltier concentric cylinder (Couette geometry: DIN rotor and standard cup) on shear rate scale [10^{-4}; 10^{3}] s^{-1}, at different temperature (15 °C, 21 °C, 25 °C, 35 °C) to mimic the microextrusion bioprinting temperature used. The obtained results allow us to define viscosity and yield stress profiles. An oscillation procedure was performed after validation of linear viscoelastic region at 1 Hz by stress variation. Storage modulus was determined using frequency variation (from 10^{-1} to 10^{2} rad.s^{-1}) on 2 mL AG-nX (n=1, 3, 5) samples before and after crosslinking.

Shear modulus determination involved Dynamic Mechanical Analysis (DMA) conducted on compact hydrogel discs with a diameter of 25 mm and a thickness of 2 mm and was obtained by applying shear strain followed by the use a second order Generalized Maxwell model [29] on the determined storage (G') and loss (G'') moduli.

To investigate viscous properties, a relaxation test was employed to ascertain $\tau_{1/2}$ and quantify short relaxation (<1 min) and long-term relaxation (>15 min) using a compression test (applied using a 20 mm-diameter geometry on hydrogels prepared in a similar manner, following confirmation of the linear viscoelastic region (between 20 and 200 Pa) over 1500s at 37 °C). This procedure has already been used in other research projects, enabling us to situate our results in relation to the state of the art [30].

2.5. Pores area analysis

AG-nX and AG-nX* (n=1,3,5) formulations were immersed in a solution of rhodamine B with a concentration of 1 µg/mL (Fluka, Monte Carlo, Monaco) for 10 min after porosity induction. Stacks with a depth of 100 µm were captured at 584 nm using a confocal microscope (Eclipse Ti2-E, Nikon, Japan). Matlab® software's "Image Processing" toolbox (R2020b) was utilized for thresholding and quantification operations. Segmentation functions ("ImAdjust and ImBinarize") and mathematical morphology functions ("ImOpen, ImClose, Bwareaopen") were employed for quantifying pore area.

2.6. Cell culture, inclusion and quantification

Human fibroblasts (primary cells, female, 45 years) were cultivated until 90% confluency. After two washes with DPBS (Thermo Scientific, USA) followed by incubation with 0.25% Trypsin/EDTA (Sigma Aldrich, St. Louis, MO) for 5 minutes at 37 °C to detach the cells from the culture flasks. Subsequently, the cell suspension underwent centrifugation at 300 RPM for 5 minutes at room temperature, and the resulting pellet was re-suspended in Dulbecco's Modified Eagle Medium (DMEM, ThermoFisher, USA) complete cell culture medium supplemented with 1% penicillin and streptomycin (Sigma, St. Louis, MO). *Re*-suspended cells were then gently included using a P1000 (Gilson, USA) in both AG-nX and AG-nX* at a concentration of 2 × 10^{5} cells/mL before microextrusion.

After crosslinking, the scaffolds were maintained in DMEM (ThermoFisher, USA) for 7 days, with the medium being changed every 2 to 3 days. For live:dead assay analysis, the scaffolds were stained with Calcein-AM (2 µM) and Propidium Iodide (4 µM) for 30 minutes at 37 °C. Following incubation, the samples were washed with DPBS and imaged using a fluorescence microscope to distinguish live cells (green fluorescence) from dead cells (red fluorescence).

Matlab® software's "Image Processing" toolbox (R2020b) was utilized for thresholding and quantifica-tion operations. Segmentation functions ("ImAdjust and ImBinarize") and quantification functions ("ImFindCircle") were employed for quantifying the quantity of cells by images (5<n<10 images by conditions).

2.7. 3D printing: microextrusion

To conduct microextrusion experiments, a DAGOMA DiscoEasy 200 printer (Dagomsa, France) was modified to adapt the machine for liquid deposition modeling (microextrusion). The software Repetier-Host (Hotworld GmbH & Co. KG, Germany) was used for slicing 3D objects, which allowed notably to define the number of layers and the mesh size of the produced scaffolds. The thermal crosslinking systems designed for thermoplastics were replaced with a mechanical extrusion system that accommodates sterile 10 cc syringe barrels (Nordson EFD, US). A Nema stepper motor (RS component, UK), connected to a screw through 3D-printed adapters produced by a Prusa i3 MK3S+ (Prusa, Czech Republic), generates force on the piston for extruding hydrogels through an 800 µm nozzle. The cartridges were maintained at the appropriate printing temperature using a precision incubator and kept within a thermo-insulating sheath. Impressions of scaffolds (rectilinear slabs, concentric circles, tubes) were carried out within 5 minutes of extraction from the incubator. For biological experiments, printing was conducted under sterile conditions, and the hydrogels were maintained at 37 °C with 5% CO_2 after crosslinking.

2.8. Dimensional fidelity measurements

Dimensional fidelity of 3D-printed scaffolds (rectilinear slabs, concentric circles, tubes) was assessed by taking measurements (n=4–5 by sample) with calipers for specific dimensions: length (X axis), width (Y axis) and height (Z axis). For the slab, the filament lengths in X and Y were measured while for the concentric circles, different radii for a given circle (r_X and r_Y) were measured, and the height of the tubes was also measured at various points, in mm. Comparison with the 3D object was then performed by calculating the absolute difference and error percentage using the Eq. (3):

$$\textbf{Error}\ (\%) = \frac{\textbf{Absolute difference}}{\textbf{Attended dimension}} \times\ 100 \quad (3)$$

2.9. Statistical analysis

Statistical analyses were performed using Graphpad Prism. Viscoelastic properties (both shear modulus and $\tau_{1/2}$) were assessed using ANOVA tests following a Shapiro–Wilk normality test, while G' before (liquid) and after (solid) crosslinking were compared using multiple unpaired t test after a Shapiro–Wilk normality test. Additionally, swelling ratio and hydrogel degradation rate comparisons between AG-nX formulations were performed also using a ANOVA tests following a Shapiro–Wilk normality test. Dimensional analysis results were also assessed using ANOVA tests following a Shapiro–Wilk normality test. Error bars denote the standard error of the mean (s.e.m.), and quantitative data were obtained from three or more independent experiments.

3. Results & discussion

3.1. Homogenization and pasteurization on AG-nX (n=1,3,5) formulations

To achieve the preparation of the three hydrogel formulations, static and dynamic homogenization methods were compared. To ensure the sterility of the mixture, two pasteurization methods for the formulations were implemented and mechanical impact of crosslinking and viscoelastic properties were also investigated. The entirety of these results is presented in Fig. 2.

The comparison between the AG powders static dissolution method (4 hours at 37 °C) and the dynamic method (50 RPM, 60 °C for 120 min) is illustrated in Fig. 2-A and B. For AG-1X and AG-3X formulations, both methods resulted in complete dissolution, as evidenced by the clear and uniform hydrogel obtained. However, formulation AG-5X exhibited the presence of clots and undissolved powder (Fig. 2-A), suggesting that at such a concentration (Alginate 5% w/v and gelatin 10% w/v), mechanical agitation and/or an increase in temperature could be necessary for complete dissolution. This hypothesis is supported by the appearance of AG-5X obtained through dynamic homogenization (Fig. 2-B). For batch uniformity, it is therefore relevant to employ a dynamic method (50 RPM, 60 °C for 120 min) for AG-nX (x=1,3,5) to ensure complete dissolution of the powders.

Regarding hydrogels sterilization, two pasteurization methods were applied to samples obtained through the dynamic method (50 RPM, 60 °C for 120 min). A rapid method (100 °C for 10 min, 50 RPM) and a conventional method (80 °C for 30 min, 50 RPM), both followed by a thermal shock in water at 0 °C for 10 min in both cases. After the hydrogels crosslinking, the appearance of formulations pasteurized using the conventional method (Fig. 2-C) and the rapid method (Fig. 2-D) were compared. A noticeable color change (more brownish) is observed with the rapid method, suggesting that the process temperature (90 °C) impacts the hydrogels. This temperature-dependent browning of biomaterials appears to be linked to the Maillard effect and the formation of Maillard reaction products (MRPs), as described in the literature [31]. It appears that a temperature exceeding 70 °C results in a loss of transparency. Additionally, brown spots were observed in all AG-nX (n=1,3,5) formulations after rapid pasteurization, whereas they were only present in AG-5X for conventional pasteurization. Both pasteurization methods allowed the hydrogels to be maintained in a DMEM medium without antibiotics for 3 days without any presence of contamination. Based on these observations, the conventional method seems to be a more appropriate choice to maximize the optical quality of the samples, validating the sterility of hydrogels pre- and post-crosslinking.

3.2. Crosslinking, shrinkage & swelling on AG-nX (n=1,3,5) formulations

3.2.1. Chelation and covalent bond induction

To limit cellular stress due to changes in the biochemical environment and avoid any risk of osmotic shock, the concentrations of crosslinking agents as well as the crosslinking time were minimized. Based on the literature [32], hydrogel crosslinking was achieved by adding a 1% Ca^{2+} (w/v) + 1% TAG (w/v) solution for 10 minutes at 37 °C.

Then, lyophilized hydrogels observation (Fig. 2-E) and then rehydrated hydrogels (Fig. 2-F) allowed quantification of the swelling capacity of the hydrogels (Fig. 2-G). Based on disc diameter, the post-crosslinking shrinkage was determined to be 13±3% for AG-1X, 6 ±2.5% for AG-3X, and 1±0.5% for AG-5X (Fig. 2-G). About the swelling, AG-1X reached a stable ratio of 23 within 10 hours, while the swelling of AG-3X and AG-5X hydrogels stabilized only after 36 hours, exhibiting ratios of 21.5 and 18, respectively. These results demonstrate a significant difference in swelling between AG-1X and AG-3X (p-value = 0.0293), as well as between AG-1X and AG-5X (p-value = 0.0098). However, there is no significant difference between AG-3X and AG-5X (p-value = 0.8931). Thus, it appears that the lower the concentration of AG, the greater the swelling ratio (notably when the network density is low like AG-1X). This illustrates the proportional relationship between the polymer concentration of a hydrogel and its proportional water-holding capacity [32]. This phenomenon can be logically observed given that the increased density of the elastic crosslinked network in the AG-3X and AG-5X conditions results in a reduced swelling capacity, constrained by the dimensions of the elastic network itself.

The least concentrated formulation (AG-1X) therefore exhibited the most significant shrinkage, as the formation of an interpenetrating double network (by chelation of the alginate and covalent bonding of the gelatin) generates a contraction, which is more pronounced when the water content is high [33].

Similarly, it appears that the concentration of AG directly impacts hydrolytic degradation over time (Fig. 2-H). Within the first week, AG-1X exhibits a mass loss of 24.7 ± 2.9%, compared to 7.6 ± 4.4% for AG-3X and 3.6 ± 2.9% for AG-5X. These trends continue, leading to a degradation rate of 42.5 ± 3.3% for AG-1X, while the more concentrated formulations demonstrate significantly lower rates: 17.4 ± 6.6% for AG-3X and 18.4 ± 3.1% for AG-5X. Thus, AG-1X degrades significantly faster than AG-3X (p-value = 0.0452) and AG-5X (p-value = 0.0359), although there is no significant difference in degradation rates between the two more concentrated formulations. These results indicate that lower concentration AG hydrogels (AG-1X) degrade more rapidly than higher concentrations (AG-3X and AG-5X) due to less dense network structures that facilitate hydrolytic attack and water penetration [34]. This behavior aligns with the consensus that increased crosslinking density in more concentrated hydrogels enhances mechanical stability and resistance to degradation, making them suitable for applications requiring longer-term stability.

To evaluate the viscoelastic behavior and the impact of Ca^{2+}-TAG crosslinking on the three AG-nX (n=1, 3, 5) formulations with the same solution, the shear storage modulus (G') was characterized before (-Liq.) and after crosslinking (-Sol.) (Fig. 2-I). It clearly appears that before crosslinking, the AG-nX (n=1, 3, 5) formulations showed increasing G' ranging from 0.1 to 100 rad.s^{-1} demonstrating their viscoelastic behaviors. At a same angular frequency value, we also demonstrated that the AG concentration play a significant role in the increasing of viscoelastic behavior. After crosslinking, the G' curves exhibited an asymptote demonstrating the existence of shear modulus when the angular frequency trend to 0.1 rad/s. These results confirm the transition of viscoelastic behavior in elasto-viscoelastic behavior commonly described in crosslinked hydrogels.

This is supported by the fact that elasticity gain (G') was observed after crosslinking (Fig. 2-J). Indeed, for a low-frequency shear of 0.1 rad.s^{-1} (when G' tends towards an asymptote corresponding to G0, the shear

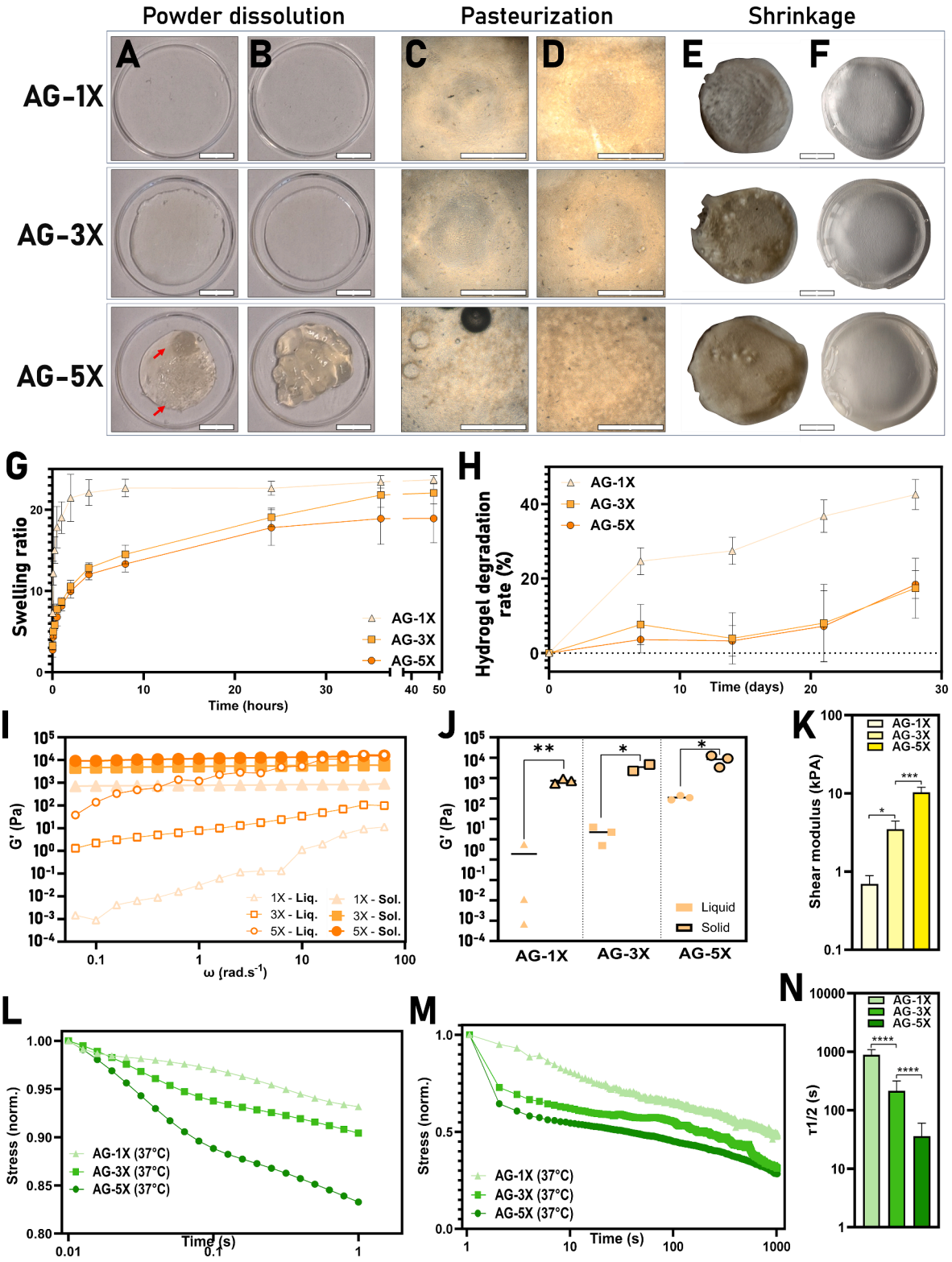

Fig. 2. Study of the preparation (dissolution, sterilization, reticulation, shrinkage) and viscoelastic properties of AG-nX (n=1,3,5) bioinks. (A) AG-nX (n=1,3,5) powders static dissolution impact on hydrogel aspect. (B) AG-nX (n=1,3,5) powders dynamic dissolution impact on hydrogel aspect. Red arrow: clots (C) Conventional pasteurization impact on hydrogel aspect. (D) Rapid pasteurization impact on hydrogel aspect. (E) Lyophilized AG-nX (n=1,3,5) crosslinked discs. (F) Rehydrated AG-nX (n=1,3,5) crosslinked discs. (G) AG-nX (n=1,3,5) swelling ability of hydrogels from a lyophilized state. (H) AG-nX (n=1,3,5) hydrogel degradation by hydrolysis over 4 weeks. AG-nX (n=1,3,5) (I) Variation of G' with shear rate [0.1–100] rad.s-1 after before (liquid) and after (solid) crosslinking at 37 °C. (J) Comparison of G' with shear rate at 0.1- rad.s-1 after before (liquid) and after (solid) crosslinking at 37 °C. (K) AG-nX (n=1,3,5) shear modulus at 37 °C. (L) AG-nX (n=1,3,5) relaxation time at 37 °C (from 0.01 to 1 s). (M) AG-nX (n=1,3,5) relaxation time at 37 °C (from 1 to 1000s). (N) AG-nX (n=1,3,5) τ1/2 at 37 °C. Scale bar = 5 mm. Results presented as mean ± SD. **: p< 0.001, *:p< 0.05 (n = 3 per condition).

modulus [35]), the comparison showed that AG-1X storage modulus went from $1.8*10^{-1}$ Pa to $7.4*10^{3}$ Pa, AG-3X G' from $2.2*10^{-0}$ Pa to $3.5*10^{4}$ Pa, and AG-5X G' from $1.1*10^{2}$ to $8.4*10^{4}$ Pa before and after crosslinking. This significant increase in elasticity reflects the formation of a crosslinked network (both ionically and chemically) in the three formulations. The higher the G' modulus, the more rigid the AG-nX (n=1,3,5) elastic solids are, indicating a direct relationship between network density and the elastic properties of the materials. Given the increasing concentrations of alginate-gelatin (a factor of 3 between AG-3X and AG-1X and a factor of 5 between AG-5X and AG-1X), the G' gaps are a direct consequence of the density of the crosslinked macromolecule network with an increase in the number of crosslinking sites. Additionally, the formulations shear moduli (G0) have been characterized (Fig. 2-K) to obtain a solid marker of elasticity, with values of 0.69 kPa for AG-1X, 3.48 kPa for AG-3X, and 10.31 kPa for AG-5X, close to the G' measured and consistent with the viscoelastic range of human tissues [36].

Another parameter related to the viscous component of AG-nX (n=1,3,5) hydrogels, static relaxation time, was characterized. The rapid static relaxation of AG-nX (n=1,3,5) presented in Fig. 2-L is such that after 1 second, AG-1X has relaxed 7% of the imposed stress, compared to 10% for AG-3X and 17% for AG-5X. Within a temporal scale of less than one second, cells interact with the AG matrix through short-term, rapid signaling involving cell adhesion molecules like integrins, crucial for initiating cell-ECM communication (these interactions promptly trigger intracellular signaling, affecting cell behavior and function [37]). As a matter of fact, the rapid relaxation of the matrix has recently been described to promote cell-material interaction, leading to cell spreading and proliferation [38]. Here, the relaxation rate of AG-nX (n=1,3,5) inversely correlates with AG concentration. Consequently, AG-1X demonstrates greater elasticity compared to AG-3X, which in turn is more elastic than AG-5X (directly proportional to their alginate-gelatin content). Therefore, cells can be presumed to interact more swiftly with AG-5X, then AG-3X, and least rapidly with AG-1X.

This property is confirmed by a longer relaxation (1000s) in Fig. 2-M, where AG-1X has relaxed 52% of the initial stress, AG-3 × 69%, and AG-5 × 72%. It is thus possible to define the $\tau_{1/2}$ at 890 s for AG-1X, 214 s for AG-3X, and 36 s for AG-5X (Fig. 2-N). This relaxation time range (up to several minutes) corresponds to other cell-matrix interactions, such as focal adhesion assembly and disassembly, mediating cell migration (spanning minutes to hours). This dynamic process is essential for cell movement and is studied extensively, for instance in the context of wound healing and cancer metastasis [39]. It thus appears that AG-5X could be a better candidate than AG-3X, itself a better candidate than AG-1X for cell proliferation and growth, thanks to its faster relaxation capabilities, as described in other studies [40,41]. Longer-term interactions (hours to days), not studied here, include differentiation and tissue remodeling, where cells remain in contact with the ECM for extended periods and even the lifespan of the cell in certain tissues [42].

These results highlight that beyond the mere concept of hydrogel "stiffness", the significant differences in stress relaxation capacity of these materials, across different temporal scales, could provide an useful tool to influence cellular fate.

These variations demonstrate that in addition to the shear modulus of each formulation (composed of the same materials but not at the same concentration), AG-nX (n=1,3,5) bioinks present significantly different viscoelastic properties that are increasing proportionally to the AG concentration. Since the biological impact of these parameters have already been described [13,27] and following the validation of the preparation and crosslinking steps, we investigated the rheological properties of AG-nX (n=1,3,5) bioinks.

3.2. Bioprintability motivated rheological investigation

The AG-nX (n=1,3,5) formulations maintain identical biochemical compositions but exhibit significantly varied concentrations. To ensure the printability of the hydrogels with and without porosity induction, rheological characterizations of the formulations were conducted. The resulting data are illustrated in Fig. 3.

Fig. 3-A represents a microextrusion device, with a nozzle from which a bioink filament is extruded. The shear rate range (10^{-1} to 10^{2} s^{-1}) used to study the viscosity of the bioinks corresponds to the shear rate applied during the bioprinting process (proportional to the pressure applied on the piston [43]). After extrusion, the rheological component of interest is the yield stress, directly related the printability of the scaffold [44].

Important differences on rheograms of AG-nX (n=1,3,5) hydrogels at 21 °C were observed in Fig. 3-B. AG-1X and AG-3X demonstrated a shear thinning profile, with viscosity values ranging from 15 to 1 $Pa.s^{-1}$ and from 5000 to 4 $Pa.s^{-1}$, respectively, for a shear rate ranging from 10^{-1} to 10^{2} s^{-1}. This non-Newtonian profile is typical of hydrogels formed from biopolymers [45,46]. In the context of microextrusion, this shear-thinning behavior is an important asset as it allows for maximizing post-printing cell viability by protecting the cells from the shear stress generated by the process [47]. AG-5X at 21 °C exhibited a gelation rate such that the rheometer torque was not powerful enough to induce rotation. It is noteworthy that over the range from 10^{-1} to 10^{2} s^{-1}, the viscosity values of AG-5X ranged from 2.5×10^{5} to 3.6×10^{5} $Pa.s^{-1}$. The viscosity of the formulations remains significant at 21 °C, notably for the AG-3X and AG-5X. Additionally, significant variations were also observed for the yield stress. Indeed, Fig. 3-E demonstrates that for a shear rate of 10^{-4} s^{-1}, the yield stress tends towards 0.03 Pa for AG-1X, 233 Pa for AG-3X, and 970 Pa for AG-5X. It has been shown that the yield stress is directly related to the printing resolution and shape fidelity in microextrusion [48]. Since AG-1X static yield stress in < 10 Pa, this formulation seems not printable at this temperature, as the hydrogel is not capable of sustaining itself under its own weight [45].

However, formulations viscosity and yield stress are modulable through temperature changes thanks to the gelatin thermo-gelling properties. Indeed, Fig. 3-C shows that at 15 °C for AG-1X, 25 °C for AG-3X, and 35 °C for AG-5X, bioinks exhibit a similar viscosity profile (between 180 and 1180 $Pa.s^{-1}$ for a shear rate of 0.1 s^{-1} up to between 2 and 5 $Pa.s^{-1}$ for a shear rate of 100 s^{-1}). It is therefore possible to obtain similar viscosity profiles for AG-nX (n=1,3,5) hydrogels, based on very different concentrations via temperature modulation. Fig. 3-C also shows that the viscosity of PEG50 depends only slightly on temperature (between 0.28 $Pa.s^{-1}$ at 30 °C and 0.48 $Pa.s^{-1}$ and 15 °C) and the material reveal a Newtonian behavior (constant viscosity) [49]. In the same way and for the same temperature variations, the yield stresses of AG-nX (n=1,3,5) range between 35 and 86 Pa for a shear rate of 10^{-4} s^{-1}, with overlapping profiles, as shown in Fig. 3-F. Then, temperature modulation allows for the adaptation of rheological properties of AG bioinks for microextrusion.

Finally, the impact of liquid-liquid emulsion on viscosity and yield stress was investigated. In this study, we have focused only on the volumetric ratio post-emulsion. Other parameters such as distribution, interconnection, and size of the pores will be investigated further. The rheological properties of the emulsion between the AG formulations and PEG present a compromise, based on the proportions and rheological properties of each component [50]. Therefore, a general decrease is observed due to porosity induction (using emulsion between AG-nX (n=1,3,5) and PEG50 at a rate of 10% v/v) while maintaining a shear thinning profile as shown in Fig. 3-D. At a given shear rate of 100 s^{-1}, AG-1X* exhibited a viscosity of 0.3 $Pa.s^{-1}$ compared to 3 $Pa.s^{-1}$ for AG-1X, AG-3X* exhibited a viscosity of 0.1 $Pa.s^{-1}$ compared to 4.5 $Pa.s^{-1}$ for AG-3X, and AG-5X* exhibited a viscosity of 0.13 $Pa.s^{-1}$ compared to 5.4 $Pa.s^{-1}$ for AG-5X. A PEG50 emulsion at a rate of 10% v/v therefore shows a significant decrease in viscosity demonstrating its role as a plasticizer. Similarly, porosity induction lowers the yield stress of AG-nX (n=1,3,5) formulations, as demonstrated in Fig. 3-G. Indeed, the yield values of porous formulations oscillate between 2 and 5 Pa for a shear

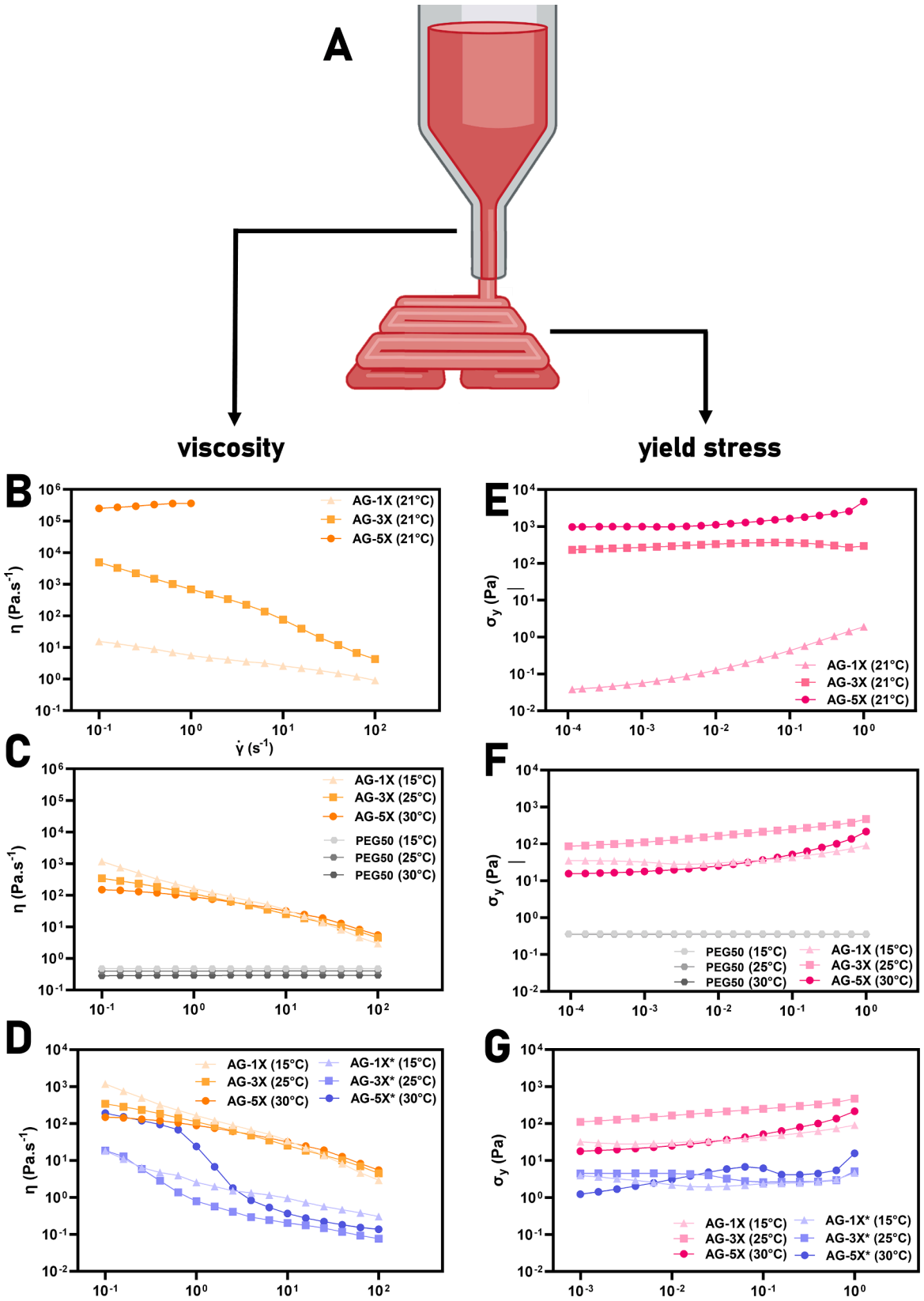

Fig. 3. AG-nX (n=1,3,5) formulations rheological properties and liquid-liquid emulsion impact. (A) Representation of a microextrusion device and a bioprinted scaffold, (B) AG-nX (n=1,3,5) viscosity at 21 °C. (C) AG-nX (n=1,3,5) viscosity at 15 °C for AG-1X*, 25 °C for AG-3X*, 30 °C for AG-5X*. (D) AG-nX (n=1,3,5) viscosity vs AG-nX* (n=1,3,5) viscosity. (E) AG-nX (n=1,3,5) yield stress at 21 °C. (F) AG-nX (n=1,3,5) yield stress at 15 °C for AG-1X & PEG50, 25 °C for AG-3X and PEG50, 30 °C for AG-5X*. (G) AG-nX (n=1,3,5) yield stress vs AG-nX* (n=1,3,5) yield stress. n = 3 per condition.

rate of 10^{-4} s^{-1}. The printability of the porous formulations seems thus more limited with this low value yield stress but remains achievable at reasonable heights (< 10 mm) [48].

3.3. Printability test

With the aim to demonstrate the ability of porous formulations to be shaped using microextrusion process, various scaffolds were produced with the AG-nX* (n=1,3,5) formulations at 10% (v/v) porosity. These results are presented in the Fig. 4.

Fig. 4-A highlights the ability of the materials to form a two-level scaffold. The microextrusion process thus enables the generation of defined macroporosity (≥ 1 mm) along the x and y axes.

Interestingly, while the differences are not statistically significant (the printed rectilinear slab demonstrated error percentages of 2.8 ± 1.7% on the X-axis and 2.6 ± 1.5% on the Y-axis for AG-5X*, compared to 1.7 ± 1.4% and 2.6 ± 2.6% for AG-3X*, and 6.6 ± 9.7% and 3.8 ± 2.2% for AG-1X*, on the X and Y axes, respectively (Fig. 4-F). Consistently with the yield stress values presented in Fig. 3-G, this suggests a potential relationship AG-nX* (n=1,3,5) bioinks concentration and printing resolution, with no notable differences between the X and Y axes.

This trend is more distinctly confirmed by the concentric discs shown in Fig. 4-B. Similarly, a proportionality between print fidelity and AG bioink (with 10% v/v porosity) is observed. As illustrated in Fig. 4-D and Table 2, error rates for the concentric circles' radii on the X and Y axes indicate an error average of 4.0 ± 3.0 % and 6.2 ± 3.2 % for AG-5X*, 8.4 ± 4.9% and 7.6 ± 5.7 % for AG-3X*, and 16.0 ± 5.3 % and 14.9 ± 5.2 % for AG-1X*, suggesting a correlation between material concentration (therefore static yield stress, Fig. 3-G) and dimensional accuracy. Based on flat scaffolds (rectilinear and concentric) observations, focused on X and Y axis fidelity, the concentric scaffold's higher error rates suggest AG-nX (n=1,3,5) bioinks have reduced resolution in multi-strand assemblies (concomitant).

Additionally, tubular scaffold of 10 mm height allowed the appreciation of the ability of the bioinks AG-nX (n=1,3,5) to form scaffolds on the Z-axis (Fig. 4-C). Here, although the threshold values of the AG-nX* (n=1,3,5) emulsified hydrogels shown in Fig. 3-G exhibit small variations, a significant impact on the print resolution of bioinks has been demonstrated. Indeed, AG-5X* (σ_y= 5 Pa) forms conforming scaffold, with only 6.9 ± 2.1 of error rate compared to the 3D file. A slight collapse is observed for AG-3X* (σ_y= 4 Pa) with an error rate of 14.7 ± 3.0 %, and a significantly important collapse of 27.6 ± 4.9 % is noted for AG-1X* (σ_y= 1 Pa) as shown in Fig. 4-D and Table 2.

These results highlight the significant sensitivity of static yield stress to changes, confirming that dimensional fidelity remains acceptable despite the yield stress reduction induced by the liquid-liquid emulsions. Notably, it appears that the resultant impact is much more pronounced on the Z-axis than on the X and Y axes, making it relevant to favor long and relatively flat scaffolds over thin and tall ones with this range of materials. These findings suggest the feasibility of creating resolutive structures with a yield stress below 10 Pa, as demonstrated by gelatin-based bioinks in existing literature [51]. We propose that the observed inaccuracies and variability in data indicating fidelity fluctuations during the process stem from a phase shift related to temperature and AG concentration. While similar phenomena have been documented in microextrusion processes [52], further investigation is warranted in this study's context.

Finally, three-fold extrusion was performed, incorporating alternating layers of the three bioinks. Fig. 4-E illustrates two flat structures (slab and concentric circle) alongside a thick scaffold comprising three layers. Despite minor variations in post-crosslinking shrinkage (Fig. 2-G), the overall resolution of the multi-material scaffolds remains qualitative. Each layer remains distinguishable, and the object maintains good integrity post-crosslinking and rinsing. Regarding isoporosity through liquid-liquid emulsion on AG-nX* (n=1,3,5) hydrogels, this possibility has been previously demonstrated [27]. Post-printing porosity (10% v/v) is depicted in Fig. 4-E, where confocal microscopy reveals the presence of microstructure in all three co-printed formulations.

3.4. Micro- & macrostructure tailoring

To assess the microscopic appearance of the AG-nX (n=1,3,5) hydrogels printed by microextrusion, the scaffolds were characterized using SEM and confocal microscopy. Biocompatibility was also investigated, along with various emulsion conditions. These results are presented in the Fig. 5.

Based on this process, two-layered bioprinted scaffolds with 1 × 1 mm meshes are presented in Fig. 5-A (here, AG-5X*). This representation allows for the appreciation of both the macro and micro-pores of this structure, obtained by microextrusion of porous bioinks.

AG-3X* filament internal microstructure is presented in Fig. 5-B. A spongy structure is visible, with an important number of variable diameter pores (without apparent interconnectivity between pores) compared to the dense hydrogel. Microstructure directly generated by the liquid-liquid emulsion process, depends on physical parameters such as the proportion between the two fluids or the mixing temperature [50]. The liquid-liquid emulsion method thus emerges as a highly interesting process for inducing porosity in hydrogels, compatible with bio-printing via microextrusion.

About other formulations, Fig. 5-C shows the presence of micropores on the surface of the printed filaments for AG-nX* compared to the dense AG-3X. It is important to keep in mind that the representation of the microstructure was relatively biased in SEM because (i) the samples were lyophilized and (ii) the surface appearance was different from the interior of the filament, but it nevertheless provided a relative representation revealing the external aspect of the scaffolds.

Additionally, AG-nX/PEG50 (n=1,3,5) ratios during emulsion impact on the final porosity are presented in Fig. 5-D for AG-3X. The pore size depended on the volume of PEG50, with median values of average surface area of 340 μm^2 with a volume of 5% v/v PEG, 1200 μm^2 for 10% v/v up to 3700 μm^2 for 20% v/v. Similarly, since temperature directly influences the viscoelastic behavior of the AG-nX (n=1, 3, 5) formulations (Fig. 2-A/B), it directly impacts the quality of the emulsion. Fig. 5-E shows that for a PEG50 fraction of 10% at 10 °C, the microstructure consisted of large pieces of AG-3X. A graphical representation of the pore size distribution as a function of the PEG50 ratio and the temperature during the emulsification of AG-5X is presented in Fig. 5-F. The shear associated with the emulsion process disrupted the gelled hydrogel (which behaves like a solid due to the strong gelation phenomenon that occurred at 10 °C). In contrast, the decrease in viscosity of the AG-3X formulation at 37 °C (behaves like a liquid) allowed for the generation of a finer emulsion, with pores of a median surface area of 370 μm^2.

This phenomenon is mostly justified by the fact that an emulsion between two fluids is viscosity-dependant [50]. Indeed, emulsion stability is significantly influenced by the viscosities of the mixed fluids; a large viscosity difference tends to produce larger droplets and less stable emulsions, as the denser fluid hinders the formation of smaller droplets. Conversely, similar viscosities between fluids facilitate the creation of stable emulsions with uniform droplet sizes due to more even shear distribution during mixing [53]. Therefore, the microstructure of AG-nX (n=1,3,5) formulations appears to be highly modifiable in terms of pore shape and diameter.

Finally, the biocompatibility of AG-nX* (n=1,3,5) and the impact of pores on cellular fate were investigated (Fig. 6).

The viability study of fibroblasts (post-emulsion inclusion and post-extrusion) in AG-3X* with a dense control is presented in Fig. 6-A, where the cells were cultured up to day 7 (D7). The Fig. 6-B shown significant proliferation under 2D conditions. Therefore, cellular proliferation was quantified under both porous and non-porous conditions.

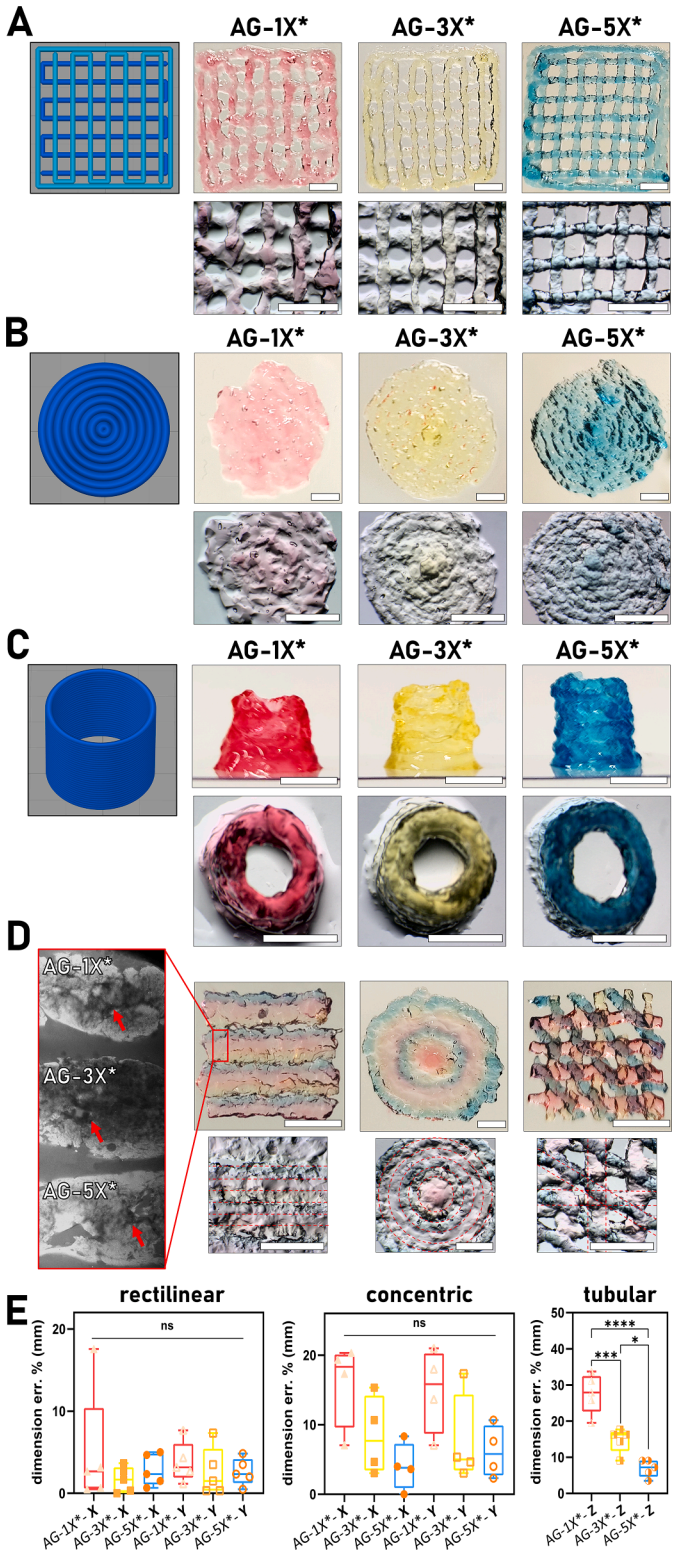

Fig. 4. Microextrusion-printed scaffolds of AG-nX* (n=1,3,5) bioinks (PEG50 10% v/v) with a 800 μm diameter nozzle at different temperature (AG-1X* at 15 °C, AG-3X* at 25 °C and AG-5X* at 30 °C) after crosslinking. (A) Flat scaffold with L=25 mm, l= 25 mm, 2 layers of 0.6 mm. (B) Circular scaffold with concentric pattern (8 layers from center) with diameter = 20 mm. (C) Tube scaffold in vase mode, height = 10 mm, layer number = 15. (D) Three-fold extrusion of AG-nX*(n=1,3,5) in slab (L=10 mm, l=10 mm, alternance of 4 AG-nX* (n=1,3,5) layers), concentric pattern (L=l= 10 mm) and 3 layers scaffold (level 1: AG-1X*, level 2: AG-3X*, 90°, level 3: AG-5X*, 45°). (E) AG-nX* (n=1,3,5) microstructure observed at confocal. Red arrow: pores. Scale bar = 5 mm. (F) Dimensional error (print fidelity) in percentage for each printed scaffold (rectilinear, concentric, tubular) along the X and Y axes. Results are presented as mean ± SD. ****: $p < 0.0001$, ***: $p < 0.001$, *: $p < 0.05$ (n = [3–5] per condition).

Table 2
Dimensional error (print fidelity) in percentage for each printed scaffold (rectilinear, concentric, tubular) along the X and Y axes. Results are presented as mean ± SD.

		X Err% (mm)	Y Err% (mm)	Z Err% (mm)
Rectilinear slab scaffold	AG-1X*	6.6 ± 9.7	3.8 ± 2.2	/
	AG-3X*	1.7 ± 1.4	2.6 ± 2.6	/
	AG-5X*	2.8 ± 1.7	2.6 ± 1.5	/
Concentric circular scaffold	AG-1X*	16.0 ± 5.3	14.9 ± 5.2	/
	AG-3X*	8.4 ± 4.9	7.6 ± 5.7	/
	AG-5X*	4.0 ± 3.0	6.2 ± 3.2	/
Tubular cylindric scaffold	AG-1X*	/	/	27.6 ± 4.9
	AG-3X*	/	/	14.7 ± 3.0
	AG-5X*	/	/	6.9 ± 2.1

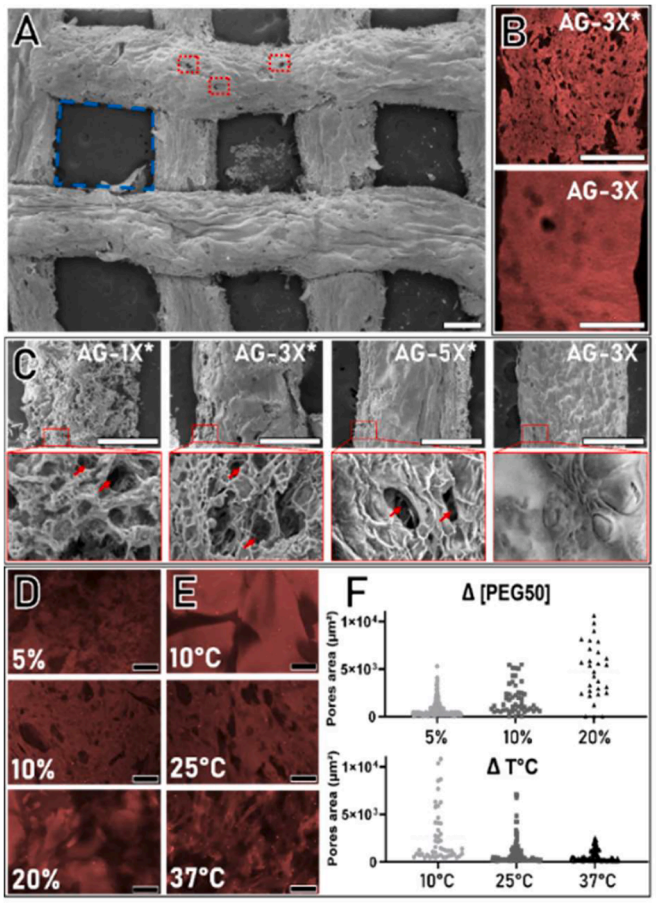

Fig. 5. AG-nX (n=1,3,5) microstructure modulation. (A) SEM observation of 3D-printed AG-5X* scaffold with macro (blue dotted squares) and micro (red dotted squares) pores. (B) Confocal observation of the microstructure with or without induction of porosity. (C) Impact of porosity induction on the appearance of 3D printed scaffolds in SEM (AG-1X*, AG-3X*, AG-5X* (10% porous) versus AG-3X (non-porous). (D) AG-3X* - PEG50 proportion impact (v/v) on pore size a 25 °C. (E) AG-3X* (PEG50 10% v/v) mixing temperature impact on pore size. (F) Summary graph of the impact of PEG50 percentage and temperature on micropore size during emulsification. White scale bar = 500 µm. Black scale bar = 100 µm. n=3 for each samples.

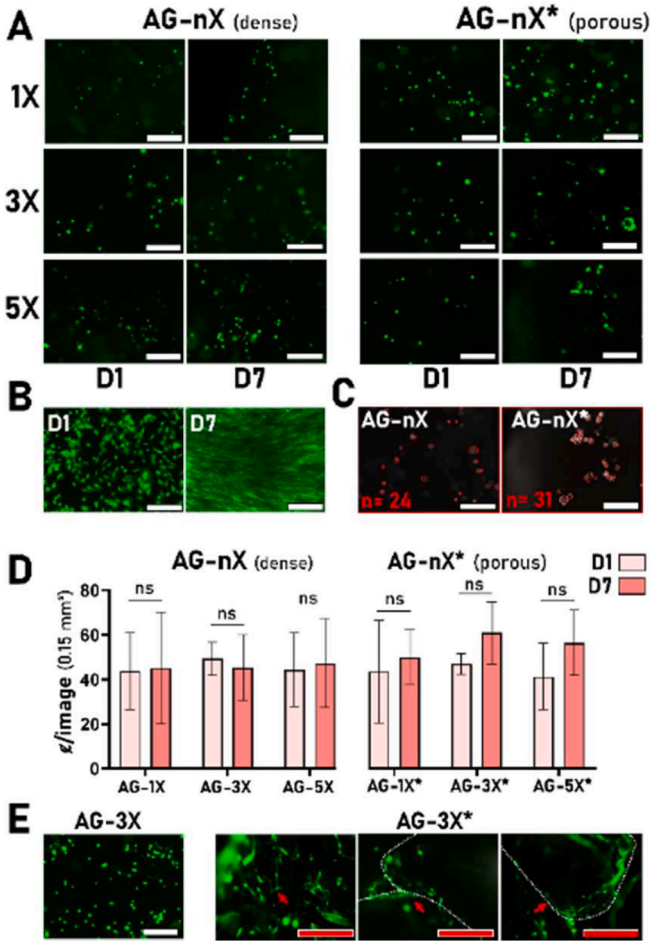

Fig. 6. Monitoring of fibroblast morphology and proliferation in dense (AG-nX) and porous (AG-nX*) hydrogels over 7 days in circular scaffolds using live-dead assay (calceine-AM and propidium iodide). (A) Observation of fibroblast proliferation in AG-nX and AG-nX* from D1 to D7. (B) Proliferation control from D1 to D7 (plastic plate). (C) Image-based cell counting method (Matlab). (D) Quantification of cell numbers for each condition (n = 3). (E) Analysis of the impact of porosity on fibroblast morphology in AG-5X dense and porous conditions at D7.

The results demonstrate a high cell viability after 7 days of culture in both conditions due to the strong calcein signal (green, viability) and negligible iodic propidium (red, necrosis), validating its high biocompatibility as previously described [53,54]. Additionally, the extrusion process didn't seem to impact cell viability in both cases. Using a cell counting method based on image processing (Fig. 6-C), quantification of cell proliferation was achieved and is shown in

Fig. 6-D. Although the analysis did not reveal a significant difference in proliferation between porous and non-porous conditions, nor between D1 and D7, all porous conditions showed a higher cell number after 7 days of culture. This suggests that the introduction of porosity in the AG-nX* formulations slightly enhance cell proliferation, likely due to the increased surface area available for interaction.

Finally, Fig. 6-E illustrates the impact of porosity in AG-5X on fibroblast morphology after 7 days of growth. In dense condition, while the cells remain viable, they retain a spherical shape under dense conditions. However, they exhibit adhesion along the cell's length and adopt a more highly spread morphology like that obtained in conventional cell culture [55], demonstrating an improved interaction between cells and available anchorage site.

[54-56] This analysis reveals that the liquid-liquid emulsion method is a promising approach for generating porous hydrogels with adjustable microstructures compatible with microextrusion as described in the literature [24], significantly impacting bioprinted scaffold porosity and biocompatibility, thereby offering enhanced cellular interactions.

4. Conclusion

This comprehensive study explores several key factors essential for successful preparation, characterization, and application of AG hydrogel formulations. Through meticulous experimentation, it was determined that dynamic homogenization methods proved superior for achieving uniform dissolution of alginate and gelatin powders, particularly evident in higher concentration formulations. Moreover, conventional pasteurization (80 °C for 30 min at 50 RPM) emerged as the preferred method for maintaining both sterility and optical quality. By optimizing crosslinking conditions, including minimizing stress-inducing factors, significant improvements in the mechanical properties of hydrogels were achieved, showcasing enhanced elasticity, and reduced post-crosslinking shrinkage. The investigation into viscoelastic behaviors further underscored the correlation between formulation concentrations and resultant properties, crucial for understanding cellular interactions and fate within the hydrogel matrix.

Furthermore, rheological studies elucidated the printability of hydrogel formulations, with temperature modulation offering a versatile approach to tailor viscosity profiles. The introduction of liquid-liquid emulsion techniques facilitated the induction of porosity, enriching scaffold architectures with microstructures conducive to cellular interactions. Importantly, biocompatibility assessments revealed the potential of porous hydrogels to foster improved cellular behaviors, promising advancements in tissue engineering applications.

Overall, this multidimensional exploration not only enhances our understanding of AG hydrogel formulations but also offers valuable insights into their versatile applications, from bioprinting to tissue engineering, ultimately contributing to the advancement of biomedical research and therapeutic interventions.

CRediT authorship contribution statement

Lucas Lemarié: Writing – review & editing, Writing – original draft, Visualization, Methodology, Investigation, Funding acquisition, Formal analysis, Data curation, Conceptualization. **Jérôme Sohier:** Writing – review & editing, Validation, Supervision, Resources, Project administration. **Edwin-Joffrey Courtial:** Writing – review & editing, Validation, Supervision, Software, Resources, Project administration.

Declaration of competing interest

The authors declare no conflict of interest or competing interests.

Data availability

Data will be made available on request.

Acknowledgment

The authors express their gratitude to the IPS-PGNM core facility (https://pgnm.inmg.fr/plateformes-inmg/, Lyon, FRANCE) for providing the AG08C5 and SCTi003-A (Stem Cell Technologies) control IPS lines. The AG08C5 line is officially registered in the European hPSCreg as PGNMi001-A (https://hpscreg.eu/cell-line/PGNMi001-A) [12]. The SCTi003-A is a commercial cell line, female, and derived from blood cells (STEMCELL, Vancouver, Canada). The authors also acknowledge that all human cells utilized at the iPS-PGNM platform are duly declared to the French Ministry of Health (CODECOH DC-2022–5055). The experiments were conducted with the invaluable assistance of the LBTI (Laboratory for Tissue Biology and Therapeutic Engineering, Lyon, France) and the academic platform 3dFAB (Villeurbanne, France).

Selected artwork shown in Fig. 1 were used adapted from pictures provided by Servier Medical Art (Servier; https://smart.servier.com/), licensed under a Creative Commons Attribution 4.0 Unported License.

Funding sources

This research received financial support from SEGULA Technologies and the ANRT (National Association for Research and Technology).

References

[1] B. Zhang, L. Gao, L. Ma, Y. Luo, H. Yang, Z. Cui, 3D bioprinting: a novel avenue for manufacturing tissues and organs, Engineering 5 (4) (2019) 777–794, https://doi.org/10.1016/j.eng.2019.03.009.
[2] S. Ramesh, et al., Extrusion bioprinting: Recent progress, challenges, and future opportunities, Bioprinting 21 (November 2020) (2021) e00116, https://doi.org/10.1016/j.bprint.2020.e00116.
[3] A. Panwar, L.P. Tan, Current status of bioinks for micro-extrusion-based 3D bioprinting, Molecules 21 (6) (2016) 685, https://doi.org/10.3390/molecules21060685. May.
[4] N. Faramarzi, et al., Patient-specific bioinks for 3D bioprinting of tissue engineering scaffolds, Adv. Healthc. Mater. 7 (11) (2018) 1–9, https://doi.org/10.1002/adhm.201701347.
[5] N. Ashammakhi, et al., Bioinks and bioprinting technologies to make heterogeneous and biomimetic tissue constructs, Mater. Today Bio. 1 (2019) 100008, https://doi.org/10.1016/j.mtbio.2019.100008.
[6] M. Di Giuseppe, et al., Mechanical behaviour of alginate-gelatin hydrogels for 3D bioprinting, J. Mech. Behav. Biomed. Mater. 79 (2018) 150–157, https://doi.org/10.1016/j.jmbbm.2017.12.018.
[7] F. Koch, K. Tröndle, G. Finkenzeller, R. Zengerle, S. Zimmermann, P. Koltay, Generic method of printing window adjustment for extrusion-based 3D-bioprinting to maintain high viability of mesenchymal stem cells in an alginate-gelatin hydrogel, Bioprinting (2020) e00094, https://doi.org/10.1016/j.bprint.2020.e00094. Aug.
[8] N. Huebsch, et al., Matrix elasticity of void-forming hydrogels controls transplanted-stem-cell-mediated bone formation, Nat Mater 14 (12) (2015) 1269–1277, https://doi.org/10.1038/nmat4407. Dec.
[9] A. Mostafavi, et al., Colloidal multiscale porous adhesive (bio)inks facilitate scaffold integration, Appl. Phys. Rev. 8 (4) (2021), https://doi.org/10.1063/5.0062823. Dec.
[10] C. Fan, D.A. Wang, Macroporous Hydrogel Scaffolds For Three-Dimensional Cell Culture and Tissue Engineering, Mary Ann Liebert Inc, 2017, https://doi.org/10.1089/ten.teb.2016.0465. Oct. 01.
[11] F. You, X. Wu, X. Chen, 3D printing of porous alginate/gelatin hydrogel scaffolds and their mechanical property characterization, Int. J. Polymer. Mater. Polymer. Biomater. 66 (6) (2017) 299–306, https://doi.org/10.1080/00914037.2016.1201830. Apr.
[12] N.F. Truong, et al., Microporous annealed particle hydrogel stiffness, void space size, and adhesion properties impact cell proliferation, cell spreading, and gene transfer, Acta Biomater. 94 (2019) 160–172, https://doi.org/10.1016/j.actbio.2019.02.054. Aug.
[13] L. Griveau, et al., Design and characterization of an in vivo injectable hydrogel with effervescently generated porosity for regenerative medicine applications, Acta Biomater. 140 (2022) 324–337, https://doi.org/10.1016/j.actbio.2021.11.036. Mar.
[14] F.J. Maksoud, et al., Porous Biomaterials For Tissue Engineering: a Review, Royal Society of Chemistry, 2022, https://doi.org/10.1039/d1tb02628c. Jul. 26.
[15] M. Dadsetan, et al., Effect of hydrogel porosity on marrow stromal cell phenotypic expression, Biomaterials 29 (14) (2008) 2193–2202, https://doi.org/10.1016/j.biomaterials.2008.01.006.
[16] Y.-C. Chiu, J.C. Larson, A. Isom, and E.M. Brey, 'Generation of Porous Poly (Ethylene Glycol) Hydrogels by Salt Leaching', 2010.

[17] C.M. Hwang, et al., Fabrication of three-dimensional porous cell-laden hydrogel for tissue engineering, Biofabrication 2 (3) (2010), https://doi.org/10.1088/1758-5082/2/3/035003. Sep.
[18] J. Grenier, H. Duval, F. Barou, P. Lv, B. David, D. Letourneur, Mechanisms of pore formation in hydrogel scaffolds textured by freeze-drying, Acta Biomater. 94 (2019) 195–203, https://doi.org/10.1016/j.actbio.2019.05.070. Aug.
[19] M. Carrancá, et al., Versatile lysine dendrigrafts and polyethylene glycol hydrogels with inherent biological properties: in vitro cell behavior modulation and in vivo biocompatibility, J. Biomed. Mater. Res. A (February) (2020) 1–12, https://doi.org/10.1002/jbm.a.37083.
[20] S. Van Vlierberghe, G.J. Graulus, S.K. Samal, I. Van Nieuwenhove, P. Dubruel, Porous hydrogel biomedical foam scaffolds for tissue repair. Biomedical Foams for Tissue Engineering Applications, Elsevier Ltd., 2014, pp. 335–390, https://doi.org/10.1533/9780857097033.2.335.
[21] J.M. Lee, E.S. Chan, R. Nagasundara Ramanan, C.W. Ooi, Liquid-liquid equilibria of aqueous two-phase systems made of polyethylene glycol and gelatin systems and their application in emulsion formation, Fluid Phase Equilib. 508 (2020), https://doi.org/10.1016/j.fluid.2019.112441. Mar.
[22] A. Sannino, et al., Synthesis and characterization of macroporous poly(ethylene glycol)-based hydrogels for tissue engineering application, J. Biomed. Mater. Res. A 79 (2) (2006) 229–236, https://doi.org/10.1002/jbm.a.30780. Nov.
[23] Z. Wang, H. Huang, Y. Wang, M. Zhou, W. Zhai, A Review of the Preparation of Porous Fibers and Porous Parts By a Novel Micro-Extrusion Foaming Technique, Multidisciplinary Digital Publishing Institute (MDPI), 2024, https://doi.org/10.3390/ma17010172. Jan. 01.
[24] G.L. Ying, et al., Aqueous two-phase emulsion bioink-enabled 3D bioprinting of porous hydrogels, Adv. Mater. 30 (50) (2018), https://doi.org/10.1002/adma.201805460. Dec.
[25] J. Jang, Y.J. Seol, H.J. Kim, J. Kundu, S.W. Kim, D.W. Cho, Effects of alginate hydrogel cross-linking density on mechanical and biological behaviors for tissue engineering, J. Mech. Behav. Biomed. Mater. 37 (2014) 69–77, https://doi.org/10.1016/j.jmbbm.2014.05.004.
[26] C.W. Yung, L.Q. Wu, J.A. Tullman, G.F. Payne, W.E. Bentley, T.A. Barbari, Transglutaminase crosslinked gelatin as a tissue engineering scaffold, J. Biomed. Mater. Res. A 83 (4) (2007) 1039–1046, https://doi.org/10.1002/jbm.a.31431. Dec.
[27] L. Lemarié, T. Dargar, I. Grosjean, V. Gache, E.J. Courtial, J. Sohier, Human Induced Pluripotent Spheroids' Growth Is Driven by Viscoelastic Properties and Macrostructure of 3D Hydrogel Environment, Bioengineering 10 (12) (2023) 1418, https://doi.org/10.3390/bioengineering10121418. Dec.
[28] N.V. Gupta and H.G. Shivakumar, 'Investigation of Swelling Behavior and Mechanical Properties of a pH-Sensitive Superporous Hydrogel Composite', 2012.
[29] E.J. Courtial, L. Fanton, M. Orkisz, P.C. Douek, L. Huet, R. Fulchiron, Hyper-Viscoelastic Behavior of Healthy Abdominal Aorta, IRBM 37 (3) (2016) 158–164, https://doi.org/10.1016/j.irbm.2016.03.007. Jun.
[30] O. Chaudhuri, et al., Hydrogels with tunable stress relaxation regulate stem cell fate and activity, Nat. Mater. 15 (3) (2016) 326–334, https://doi.org/10.1038/nmat4489.
[31] L. Khadidja, C. Asma, B. Mahmoud, E. Meriem, Alginate/gelatin crosslinked system through Maillard reaction: preparation, characterization and biological properties, Polym. Bull. 74 (12) (2017) 4899–4919, https://doi.org/10.1007/s00289-017-1997-z. Dec.
[32] N. Pilipenko, et al., Tailoring swelling of alginate-gelatin hydrogel microspheres by crosslinking with calcium chloride combined with transglutaminase, Carbohydr. Polym. 223 (2019), https://doi.org/10.1016/j.carbpol.2019.115035. Nov.
[33] M. Wang, W. Li, G. Tang, C.E. Garciamendez-Mijares, Y.S. Zhang, Engineering (Bio)Materials Through Shrinkage and Expansion, John Wiley and Sons Inc, 2021, https://doi.org/10.1002/adhm.202100380. Jul. 01.
[34] J.L. Drury, D.J. Mooney, Hydrogels For Tissue engineering: Scaffold design Variables and Applications, Elsevier BV, 2003, https://doi.org/10.1016/S0142-9612(03)00340-5.
[35] E.-J. Courtial, 'Elaboration de matériaux silicone au comportement mécanique adapté pour la réalisation de fantômes aortiques patients-spécifiques', 2015.
[36] A.M. Handorf, Y. Zhou, M.A. Halanski, W.J. Li, Tissue Stiffness Dictates development, homeostasis, and Disease Progression, Taylor and Francis Inc, 2015, https://doi.org/10.1080/15476278.2015.1019687. Jan. 01.
[37] Richard O. Hynes, 'Integrins: Bidirectional, Allosteric Signaling Machines', 2002.
[38] O. Chaudhuri, J. Cooper-White, P.A. Janmey, D.J. Mooney, V.B. Shenoy, Effects of extracellular matrix viscoelasticity on cellular behaviour, Nat. Res. (2020), https://doi.org/10.1038/s41586-020-2612-2.
[39] B. Geiger, J.P. Spatz, and A.D. Bershadsky, 'Environmental sensing through focal adhesions', Jan. 2009. doi: 10.1038/nrm2593.
[40] A. Bauer, et al., Hydrogel substrate stress-relaxation regulates the spreading and proliferation of mouse myoblasts, Acta Biomater. 62 (2017) 82–90, https://doi.org/10.1016/j.actbio.2017.08.041. Oct.
[41] J. Hazur, N. Endrizzi, D.W. Schubert, A.R. Boccaccini, B. Fabry, Stress relaxation amplitude of hydrogels determines migration, proliferation, and morphology of cells in 3-D, bioRxiv (2021), https://doi.org/10.1101/2021.07.08.451608.
[42] D.E. Discher, D.J. Mooney, and P.W. Zandstra, 'Growth factors, matrices, and forces combine and control stem cells', Jun. 26, 2009. doi: 10.1126/science.1171643.
[43] A. Blaeser, D.F. Duarte Campos, U. Puster, W. Richtering, M.M. Stevens, H. Fischer, Controlling Shear Stress in 3D Bioprinting is a Key Factor to Balance Printing Resolution and Stem Cell Integrity, Adv. Healthc. Mater. 5 (3) (2016) 326–333, https://doi.org/10.1002/adhm.201500677.
[44] A. Lopez, C.A. Marquette, E.J. Courtial, FingerMap: a new approach to predict soft material 3D objects printability, Progr. Addit. Manuf. (0123456789) (2020), https://doi.org/10.1007/s40964-020-00143-5.
[45] S. Ji, M. Guvendiren, Recent advances in bioink design for 3D bioprinting of tissues and organs, Front. Bioeng. Biotechnol. 5 (APR) (2017) 1–8, https://doi.org/10.3389/fbioe.2017.00023.
[46] M. Guvendiren, H.D. Lu, and J.A. Burdick, 'Shear-thinning hydrogels for biomedical applications', Jan. 14, 2012. doi: 10.1039/c1sm06513k.
[47] L. Lemarié, A. Aravind, P. Emma, M. Christophe, and C. Edwin-joffrey, 'Bioprinting Rheology, simulation and data analysis toward bioprinting cell viability awareness', vol. 21, no. December 2020, 2021, doi: 10.1016/j.bprint.2020.e00119.
[48] E.J. Courtial, et al., Silicone rheological behavior modification for 3D printing: Evaluation of yield stress impact on printed object properties, Addit. Manuf. 28 (March) (2019) 50–57, https://doi.org/10.1016/j.addma.2019.04.006.
[49] M. Cherecheş, C. Ibanescu, M. Danu, E.I. Cherecheş, A.A. Minea, PEG 400-Based phase change materials Nano-Enhanced with Alumina: An experimental approach, Alexand. Eng. J. 61 (9) (2022) 6819–6830, https://doi.org/10.1016/j.aej.2021.12.029. Sep.
[50] D.G.T. Strange, M.L. Oyen, Composite hydrogels for nucleus pulposus tissue engineering, J. Mech. Behav. Biomed. Mater. 11 (2012) 16–26, https://doi.org/10.1016/j.jmbbm.2011.10.003. Jul.
[51] V.H.M. Mouser, F.P.W. Melchels, J. Visser, W.J.A. Dhert, D. Gawlitta, J. Malda, Yield stress determines bioprintability of hydrogels based on gelatin-methacryloyl and gellan gum for cartilage bioprinting, Biofabrication 8 (3) (2016), https://doi.org/10.1088/1758-5090/8/3/035003. Jul.
[52] S. Freeman, S. Calabro, R. Williams, S. Jin, K. Ye, Bioink Formulation and Machine Learning-Empowered Bioprinting Optimization, Frontiers Media S.A, 2022, https://doi.org/10.3389/fbioe.2022.913579. Jun. 13.
[53] S. Tesch and H. Schubert, 'Influence of increasing viscosity of the aqueous phase on the short-term stability of protein stabilized emulsions'. [Online]. Available: www.elsevier.com/locate/jfoodeng.
[54] L.J. Pourchet, et al., Human skin 3D bioprinting using scaffold-free approach, Adv. Healthc. Mater. 6 (4) (2017) 1–8, https://doi.org/10.1002/adhm.201601101.
[55] N. Soltan, L. Ning, F. Mohabatpour, P. Papagerakis, X. Chen, Printability and Cell Viability in Bioprinting Alginate Dialdehyde-Gelatin Scaffolds, ACS Biomater. Sci. Eng. 5 (6) (2019) 2976–2987, https://doi.org/10.1021/acsbiomaterials.9b00167.
[56] E. Middelkoop, 'Fibroblast phenotypes and their relevance for wound healing', Mar. 2005. doi: 10.1177/1534734605275174.